photonics

MDPI

Article

Design of Terahertz Polarization-Multiplexed Structured Light Metasurface Based on Particle Swarm Optimization

Siyuan Cheng †, Guangyi Zhang † and Tao Ju *

Guangxi Key Laboratory of Optoelectronic Information Processing, School of Optoelectronic Engineering, Guilin University of Electronic Technology, Guilin 541004, China; csy136377@163.com (S.C.); 18066575310@163.com (G.Z.)

* Correspondence: wf-jutao@163.com

† These authors contributed equally to this work.

Abstract

We propose a terahertz achromatic polarization-multiplexed structured light metasurface based on the particle swarm optimization (PSO) algorithm, operating from 0.8 to 0.95 THz. A dielectric silicon meta-atom array combined with propagation phase modulation is employed to achieve broadband wavefront control under two orthogonal linear polarizations. By constructing a phase-response database and using PSO for global optimization of phase compensation factors at multiple frequencies, the metasurface simultaneously satisfies different target phase profiles while suppressing chromatic aberration. Two multifunctional devices are designed. The first generates a conventional focused spot under *x*-polarized incidence and a first-order Bessel beam under *y*-polarized incidence. The second produces a focused vortex beam with topological charge $l = 1$ under *x* polarization and a focused vortex beam with $l = 2$ under *y* polarization. Full-wave simulations demonstrate stable focal positions, low inter-channel crosstalk, and good achromatic performance across the operating band. The Bessel beam preserves its nondiffracting core, while both vortex channels exhibit clear phase singularities and well-defined orbital angular momentum states. Most operating frequencies maintain relatively high focusing efficiency. Compared with conventional cascaded optical components, our design provides a compact and stable platform for terahertz structured light generation, orbital angular momentum multiplexing, nondiffracting imaging, and multidimensional polarization information processing.

Keywords: terahertz metasurface; polarization multiplexing; particle swarm optimization

1. Introduction

The manipulation of multiple degrees of freedom of electromagnetic waves, including polarization, phase, and spatial mode, is of central importance for advanced terahertz systems [1–3]. Structured light fields [4], such as vortex beams [5–7] carrying orbital angular momentum and nondiffracting Bessel beams [8–10], enable additional information channels and enhanced flexibility in wavefront engineering. Despite these advantages, conventional implementations in the terahertz regime typically rely on cascaded bulk optical elements, which impose limitations on system integration and stability. These limitations become particularly critical when broadband operation and polarization multiplexing are required simultaneously. For example, vortex beams enable mode multiplexing [11–13] through different topological charges, thereby significantly increasing communication channel capacity, while Bessel beams possess long focal depth and self-healing properties [14],

Check for updates

Received: 23 April 2026
Revised: 6 May 2026
Accepted: 7 May 2026
Published: 11 May 2026

Copyright: © 2026 by the authors. Licensee MDPI, Basel, Switzerland. This article is an open access article distributed under the terms and conditions of the Creative Commons Attribution (CC BY) license.

making them attractive for terahertz tomography and particle manipulation. Therefore, developing compact and multifunctional platforms capable of generating structured light across a wide frequency range remains an open challenge in terahertz photonics. Such limitations hinder the miniaturization, integration, and multifunctional development of terahertz structured light systems.

Metasurfaces [15–17], composed of subwavelength artificial structures, provide an effective platform for tailoring electromagnetic responses within an ultrathin form factor. By engineering the local response of individual meta-atoms, it is possible to achieve precise control over phase and polarization, enabling compact implementations of complex optical functionalities. Significant progress has been achieved in metalenses, holography, polarization conversion, and dispersion engineering [18–20]. In parallel, graphene-based terahertz perfect absorbers with broadband, tunable, and multi-band sensing capabilities have also been extensively studied [21–23]. In the terahertz regime, all-dielectric metasurfaces [24–26] based on materials such as silicon, sapphire, and titanium dioxide have become promising platforms for high-performance devices because of their low loss, high refractive index, and good fabrication compatibility. In particular, crystalline silicon exhibits extremely low absorption loss and high refractive-index contrast in the terahertz band, providing a solid foundation for efficient, broadband, and polarization-controllable structured light metasurfaces.

Among various structured light fields, vortex beams and Bessel beams are two representative research directions. A vortex beam carries a helical phase factor $\exp(il\varphi)$, where l is the topological charge, and each photon carries an OAM of $l\hbar$. Such beams have important applications in optical communications, near-diffraction-limited imaging, quantum information processing, and optical micromanipulation. However, conventionally generated vortex beams are usually restricted to a specific wavelength and fixed topological charge, making it difficult to maintain high mode purity over a broadband range. On the other hand, Bessel beams are known for their nondiffracting and self-reconstructing properties. Their transverse field distribution follows the first-kind Bessel function, allowing the central spot size to remain nearly unchanged over a certain propagation distance. Bessel beams have shown unique advantages in terahertz imaging, laser processing, and optical trapping. Nevertheless, conventional Bessel beam generators such as axicons suffer from severe axial dispersion, low efficiency, and poor integrability. More importantly, practical systems often require switching or simultaneous generation of vortex and Bessel modes under different polarization states, which places higher demands on polarization multiplexing capability. In addition to passive wavefront shaping, tunable and active metasurfaces have attracted considerable attention for enabling dynamic control over terahertz waves. For instance, liquid crystal-based tunable negative-index metamaterials have been demonstrated at terahertz frequencies [27], and active terahertz metasurfaces have been explored for compact isolation applications [28]. Although the present work focuses on a passive, polarization-multiplexed achromatic design, the inclusion of active materials or external tuning mechanisms represents a promising direction for future extensions, potentially enabling reconfigurable structured light generation.

Meanwhile, dispersion engineering is a key issue in metasurface design. Since the phase response of metasurface unit cells is strongly wavelength-dependent, a single metasurface often exhibits significant chromatic aberration at different frequencies, leading to focal shift, reduced vortex mode purity, or distorted axial intensity distribution of Bessel beams. To achieve broadband achromatic performance, various strategies combining geometric phase, propagation phase, and resonance phase have been proposed. However, most existing approaches are limited to single polarization or single functionality, making them difficult to extend to polarization-multiplexed structured light applications. Therefore,

designing a terahertz metasurface that simultaneously supports polarization multiplexing, dual-mode structured light generation, and broadband achromatic performance remains a significant challenge.

To address this multi-objective and highly constrained optimization problem, conventional analytical methods or parameter-sweeping approaches are usually inefficient and prone to local optima. Intelligent optimization algorithms, especially particle swarm optimization [29–31] (PSO), have recently been introduced into inverse metasurface design due to their efficient searching capability in nonlinear high-dimensional spaces. By simulating information sharing and cooperation among individuals in a swarm, PSO can globally optimize unit cell geometries or phase distributions with relatively low computational cost, thereby satisfying multiple polarization channels, multiple frequency points, and multiple structured light design targets simultaneously. Compared with gradient-based or exhaustive search methods, PSO demonstrates stronger robustness and higher design flexibility for strongly coupled multi-objective phase-control problems.

To overcome the limitations of single-polarization, narrow-band, or single-function terahertz metasurfaces, here we present a polarization-multiplexed achromatic metasurface capable of generating distinct structured light fields under orthogonal linear polarizations across the 0.8–0.95 THz band. Using all-dielectric silicon meta-atoms, the device employs a propagation-phase modulation mechanism. A PSO algorithm is introduced to globally optimize the phase compensation coefficients at four discrete frequencies (0.8, 0.85, 0.9, 0.95 THz), thereby satisfying two independent phase profiles simultaneously while suppressing chromatic aberration. Based on this strategy, we design two dual-channel devices: one for a conventional focused spot under x-polarization and a first-order Bessel beam under y-polarization, and the other for focused vortex beam with topological charge of 1 under x-polarization and a vortex beam with charge of 2 under y-polarization. Full-wave simulations confirm stable focal positions, low inter-channel crosstalk, preserved phase singularities, and near-diffraction-limited transverse resolution across the entire working bandwidth. This work provides a new pathway toward compact and integrated terahertz structured light generation and polarization-multiplexed multifunctional systems.

2. Materials and Methods

To realize broadband polarization-multiplexed structured light manipulation in the terahertz regime, the designed metasurface is required to simultaneously control the propagation phase, polarization response, and frequency-dispersion characteristics of the incident wave at the subwavelength scale. Unlike conventional bulk optical components that rely on phase accumulation along the propagation path, metasurfaces employ artificially engineered microstructures arranged in space to introduce abrupt phase discontinuities at the interface, thereby enabling wavefront reconstruction on an ultrathin planar device. According to the generalized Snell's law [32–34], arbitrary phase gradients can be introduced by tailoring the geometric parameters and spatial orientations of subwavelength structures, allowing for flexible shaping of the transmitted wavefront. In this work, the propagation-phase modulation mechanism is adopted. Its physical principle is analogous to that of conventional lenses based on optical-path phase accumulation: In the terahertz regime, dielectric materials exhibit relatively low absorption losses, which makes the propagation-phase mechanism particularly attractive. For a meta-atom with a fixed height d, the transmitted phase shift can be expressed as [35]:

$$\phi = \frac{2\pi}{\lambda} n\, d \tag{1}$$

where λ is the wavelength of the incident wave, and n depends on the transverse geometric parameters—specifically, the major and minor axes for elliptical or rectangular cross-sections. Therefore, to realize the required phase distribution $\Phi(x,y,\lambda)$ for the target wavefront, modulation can only be achieved by varying the effective refractive index n of the microstructures at different spatial positions. The effective refractive index n is determined by the geometric parameters of each meta-atom, such as the major axis, minor axis, period, and rotation angle. For the unit located at the planar coordinate (x,y) of the metasurface, the target phase can generally be expressed as the phase difference between the desired output wavefront and a reference plane wave, which can be expressed as [36]:

$$\boldsymbol{\phi}(\boldsymbol{x},\boldsymbol{y},\boldsymbol{\lambda}) = \boldsymbol{\phi_i}(\boldsymbol{x},\boldsymbol{y},\boldsymbol{\lambda}) + \boldsymbol{C}(\boldsymbol{\lambda}) \tag{2}$$

where $\phi_i(x,y,\lambda)$ denotes the target wavefront phase function, and $c(\lambda)$ represents a constant phase compensation term. By assigning different phase responses to individual meta-atoms, multiple optical functionalities can be realized, including focusing, vortex-beam generation, and Bessel beam formation. A focused vortex beam simultaneously possesses the converging property of a spherical wave and the orbital angular momentum induced by a helical phase profile. Its ideal phase distribution, $\phi_v(x,y,\lambda)$, can be expressed as [37]:

$$\boldsymbol{\phi_v}(\boldsymbol{x},\boldsymbol{y},\boldsymbol{\lambda}) = -\frac{\boldsymbol{2\pi}}{\boldsymbol{\lambda}}\left(\sqrt{\boldsymbol{x^2}+\boldsymbol{y^2}+\boldsymbol{f^2}}-\boldsymbol{f}\right)+\boldsymbol{l\theta} \tag{3}$$

where f is the designed focal length, l is the topological charge, and $\theta = \arctan(y/x)$ is the azimuthal angle. The first term on the right-hand side of the equation represents the focusing phase term, while the second term corresponds to the helical phase term. Bessel beams are well known for their nondiffracting propagation and self-healing properties, and their ideal phase distribution, $\phi_b(x,y,\lambda)$, can be expressed as [38]:

$$\boldsymbol{\phi_b}(\boldsymbol{x},\boldsymbol{y},\boldsymbol{\lambda}) = \frac{\boldsymbol{2\pi}}{\boldsymbol{\lambda}}\sqrt{\boldsymbol{x^2}+\boldsymbol{y^2}}\boldsymbol{\sin\alpha}+\boldsymbol{l\theta} \tag{4}$$

where α is the equivalent axicon angle, which determines the central spot size and the nondiffracting propagation distance of the Bessel beam, and l is the Bessel order. In this work, a polarization multiplexing design strategy is adopted, requiring the metasurface to generate different target wavefronts under two orthogonal linear polarization incidences (x- and y-polarized light). Specifically, the x-polarized channel corresponds to $\phi_x(x,y,\lambda)$, while the y-polarized channel corresponds to $\phi_y(x,y,\lambda)$. Therefore, each metasurface unit must simultaneously provide independent phase modulation capabilities for the two polarization channels and maintain stable phase responses over the frequency range of 0.8–0.95 THz so as to suppress mode distortion caused by dispersion and achieve broadband achromatic performance.

Since dual-polarization, multi-frequency, and multifunctional wavefront control constitutes a typical high-dimensional nonlinear coupled optimization problem, conventional parameter-sweeping methods usually require enormous computational cost and are difficult to converge to the global optimum. To address this issue, the PSO algorithm is introduced for the inverse design of unit cell structural parameters, as illustrated in Figure 1.

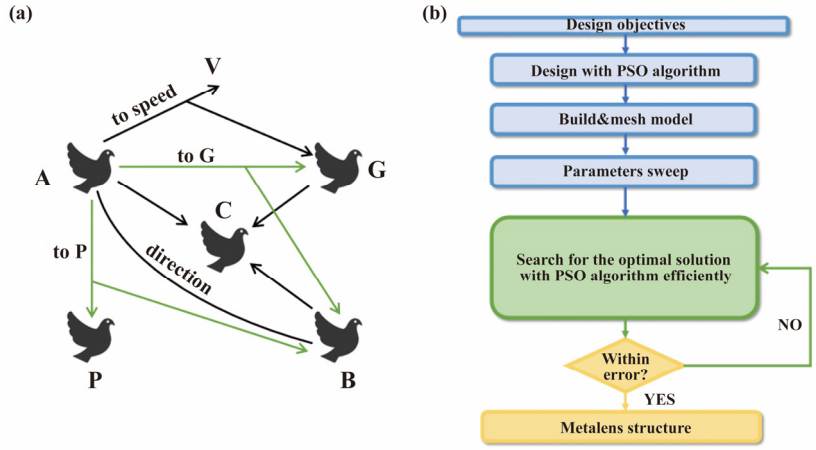


Figure 1. PSO algorithm model: (**a**) particles group model; (**b**) workflow diagram of the PSO algorithm.

As a classic swarm intelligence method, PSO emulates social behavior patterns observed in natural biological systems. In the context of metasurface inverse design, each particle represents a candidate solution corresponding to a specific set of phase compensation coefficients. Its core concept is inspired by the foraging behavior of bird flocks or fish schools: each individual in the swarm (particle) continuously adjusts its position and velocity in the search space through self-experience and shared group information, eventually converging to the optimal solution of the problem. Compared with conventional gradient-descent or exhaustive search methods, PSO offers several advantages, including fewer adjustable parameters, strong global search capability, and fast convergence speed. It is particularly suitable for solving multi-objective and strongly coupled optimization problems such as phase matching.

In the PSO algorithm, each particle represents a potential design solution, and its position in the search space corresponds to a set of structural parameters of the metasurface unit cell. The particle dynamically updates its moving velocity and direction according to its individual best historical position p and the global best historical position g of the swarm. For the i-th particle at the t-th iteration, the velocity and position update equations can be expressed as [35]:

$$\begin{aligned} v_i^{t+1} &= \omega v_i^t + c_1 r_1 (p_i - x_i^t) + c_2 r_2 (g - x_i^t) \\ x_i^{t+1} &= x_i^t + v_i^{t+1} \end{aligned} \tag{5}$$

where v^t denotes the current velocity of the particle, x^t represents its current position, ω is the inertia weight (used to balance global exploration and local exploitation abilities), c_1 and c_2 are learning factors, and r_1 and r_2 are random numbers within the interval [0, 1], introduced to enhance the stochasticity and diversity of the search process. In this design, the particle position vector specifically corresponds to the optimization variables, the phase compensation coefficients $c(\lambda)$ at different wavelengths.

We employ the finite-difference time-domain [39,40] (FDTD) method as implemented in Lumerical FDTD Solutions (version 2020 R2) to simulate silicon (Si) rectangular meta-atoms arranged on a square lattice with a periodicity of 160 μm and a height of 240 μm, placed on a 500 μm thick SiO_2 substrate.

The material properties of silicon (Si) and silicon dioxide (SiO_2) were obtained from the built-in Palik database [41] in Lumerical FDTD Solutions. These optical constants are implemented using fitted dispersive models, enabling continuous interpolation of the

complex refractive index over the frequency range of interest. Therefore, both material dispersion and absorption losses are inherently taken into account in the simulations.

To construct the electromagnetic response database, the geometric parameters of the meta-atoms are sampled over a wide range. Specifically, the length and width vary from 16 μm to 144 μm, and each dimension is discretized into 200 sampling points, leading to a total of 40,000 configurations. For each configuration, polarization-dependent transmission phase and amplitude are calculated at four frequencies, namely, 0.8, 0.85, 0.9, and 0.95 THz, forming a multi-frequency response dataset, as shown in Figure 2c,d. Based on these results, the phase response and transmission efficiency under x- and y-polarized excitations are extracted at each frequency point. To quantitatively evaluate the performance of each particle and guide the swarm toward the optimal solution, a multi-objective constrained fitness function is constructed, which is defined as follows:

$$\text{Fitness} = w_1 E_\phi + w_2 E_T + w_3 E_c \tag{6}$$

where (E_ϕ) denotes the phase error term, which quantifies the total deviation between the actual phase distribution generated by the current phase compensation coefficients and the target phase distribution under different frequency points and polarization conditions. (E_T) represents the transmission efficiency loss term, which penalizes unit configurations with low transmission efficiency. (E_c) is the broadband dispersion constraint term, measuring the inconsistency of phase responses across different frequency points. (w_1), (w_2), and (w_3) are weighting coefficients used to balance the relative importance of different optimization objectives. Through iterative execution of velocity update, position update, and fitness evaluation, the PSO algorithm is able to automatically search within the given phase compensation space and obtain an optimal set of $c(\lambda)$ combinations, ensuring that the generated wavefronts at different frequency points closely match the desired target wavefronts. Subsequently, based on the optimized phase distribution, the corresponding meta-atom geometries are selected from a pre-established database that maps structural parameters (major axis (L), minor axis (W)) to phase and transmission responses. The unit cells whose responses best match the required phase values are then arranged spatially to complete the metasurface design. Compared with conventional manual parameter sweeping methods, this approach significantly enhances the capability to solve complex multi-constraint optimization problems.

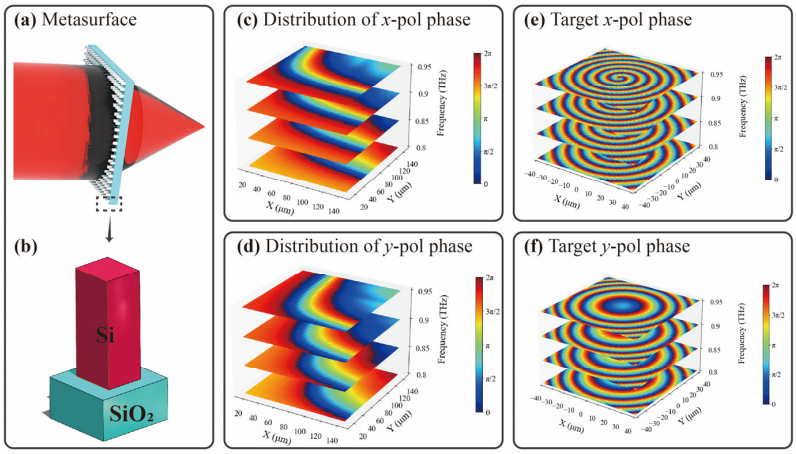


Figure 2. (**a**) Schematic diagram of the metasurface. (**b**) Schematic illustration of the metasurface unit cell. (**c**) Phase distribution under x-polarized incidence from 0.8 to 0.95 THz. (**d**) Phase distribution under y-polarized incidence from 0.8 to 0.95 THz. (**e**) Target phase under x-polarized incidence. (**f**) Target phase under y-polarized incidence.

To make the simulations computationally efficient, several idealizations were adopted. The meta-atoms were modeled with ideal geometries without considering fabrication imperfections such as dimensional deviations, edge roughness, or sidewall tapering. The materials were assumed to be homogeneous and isotropic, and perfect interfaces were considered. In addition, periodic boundary conditions were used during unit cell characterization, neglecting finite-size and edge effects. These assumptions are commonly adopted in metasurface simulations and allow us to focus on the intrinsic electromagnetic response of the structure.

3. Results and Discussion

The excitation source in the simulation is chosen as a total-field scattered-field (TFSF) source. The injection plane is at $z = -1$ μm, giving a source-to-structure distance of 1 μm. Stretched coordinate perfectly matched layers (SC-PML) with eight layers (effective thickness: ~40 μm) are applied in the x,y, and z directions as boundary conditions, placed 100 μm away from the outermost meta-atoms, to absorb outgoing waves and minimize spurious reflections from the simulation boundaries. The global mesh accuracy is set to level 4 to achieve a balance between computational accuracy and resource consumption. In addition, a frequency-domain monitor is placed at a subwavelength distance (1 μm) from the metasurface to capture the near-field distribution, enabling further analysis of the phase information and evaluation of the phase modulation characteristics of the structure at the operating wavelength.

The swarm size of 30 and the maximum iteration number of 200 are chosen based on common practice in metasurface inverse design using PSO [29–31], which ensures a balance between computational cost and convergence reliability. Preliminary trial runs confirmed that further increasing these parameters does not lead to noticeable improvement in the fitness value.

The weighting coefficients are empirically set to $w_1 = 0.8$, $w_2 = 0.15$, and $w_3 = 0.05$ to prioritize phase accuracy as the primary objective, while maintaining reasonable transmission efficiency and broadband phase consistency. The results are robust against moderate variations in these weights.

After 200 iterations, we successfully obtained an achromatic polarization-multiplexed metasurface structure exhibiting optimal performance across eight frequency points, as shown in Figure 3. Through full-wave FDTD simulations, the near-field phase distributions are obtained: under x-polarized incidence, a focusing phase profile is observed, while under y-polarized incidence, a first-order Bessel phase profile is generated.

Full-wave simulations of the far-field performance indicate that under x-polarized incidence, the focal peak position remains stably located at 8.5 mm, with a numerical aperture (NA) of 0.426, as shown in Figure 4b. Here, the focusing efficiency is defined as the ratio of the optical power confined within a region of three times the full width at half maximum ($3 \times FWHM$) around the focal spot in the focal plane to the total incident power.

In terms of focusing efficiency, except for the 0.95 THz case, where the efficiency decreases to 61.9% due to enhanced dielectric dispersion of the material, the efficiencies across the remaining operating frequencies (0.8–0.9 THz) are all above 76%, reaching a maximum of 78.2% at 0.85 THz. This demonstrates that the proposed metasurface maintains high energy utilization over most of the operating bandwidth. Meanwhile, the axial deviation of the focal position across all frequency points is less than 0.2 mm, indicating excellent achromatic focusing performance. Further analysis of the transverse resolution, as shown in Figure 4c, reveals that the full width at half maximum ($FWHM$) varies from 1.00 mm to 0.85 mm over the 0.8–0.95 THz range, increasing monotonically with wavelength, which is consistent with diffraction theory predictions.

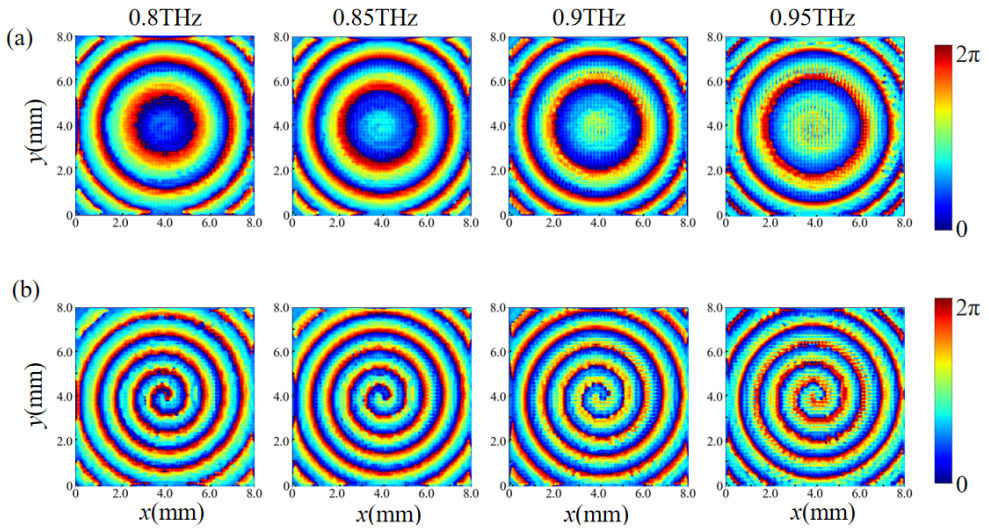


Figure 3. Near-field phase distributions of the metasurface under different polarization states from 0.8 to 0.95 THz obtained by full-wave simulations: (**a**) achromatic focusing phase distribution under *x*-polarized incidence; (**b**) achromatic Bessel phase distribution under *y*-polarized incidence.

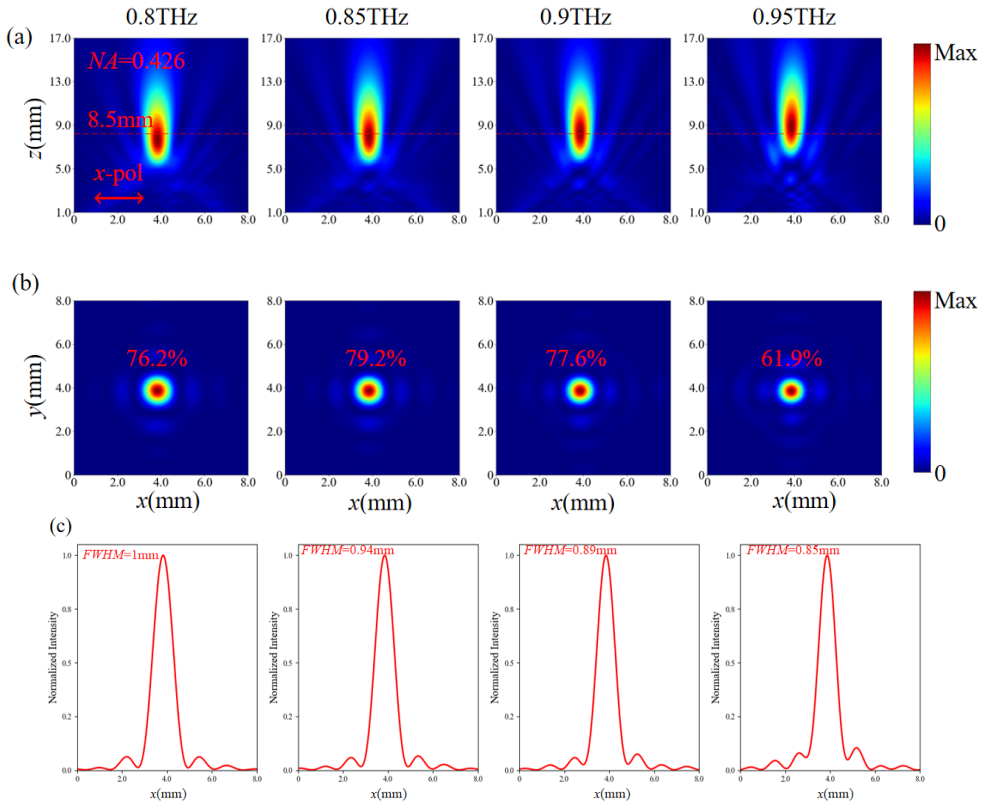


Figure 4. Full-wave simulation results of the designed metasurface under *x*-polarized incidence at different frequencies. (**a**) Energy field distributions in the x–z plane at y = 0 mm for different frequencies, showing the focal line (red). (**b**) Energy field distributions in the x–y plane at z = 8.5 mm for different frequencies, with the corresponding focusing efficiencies annotated in red. (**c**) *FWHM* and intensity distributions of the focusing lens at different frequencies.

We aim to generate a first-order Bessel beam under *y*-polarized incidence. When illuminated by *y*-polarized light, the metasurface achieves precise focal control at the designed axial position of 6.5 mm, as shown in Figure 5a. Across all operating frequencies, the intensity peak remains well aligned with the target focal position, demonstrating stable achromatic performance. Based on the metasurface diameter (7.5 mm) and focal length

(6.5 mm), the *NA* is calculated to be as high as 0.524, which is larger than that of the *x*-polarization channel (*NA* = 0.426), indicating stronger optical field confinement and enabling a smaller transverse spot size. Although the Bessel beam generation efficiency varies from 67.7% at 0.8 THz to 34.6% at 0.95 THz, this trend is primarily attributed to the enhanced dielectric dispersion of silicon in the higher THz frequency range, which shifts the resonant response of the unit cells away from the optimal operating condition and consequently reduces the transmission efficiency. Notably, across all frequencies, the central spot *FWHM* of the Bessel beam ranges from 0.656 mm to 0.735 mm, exhibiting a slight increase with increasing wavelength, which is consistent with theoretical expectations. Meanwhile, the transverse intensity profiles exhibit the characteristic features of a first-order Bessel function, including a central null and a prominent first side lobe. Although a slight degradation in side-lobe symmetry is observed at 0.85 THz and 0.95 THz, the nondiffracting core remains well preserved.

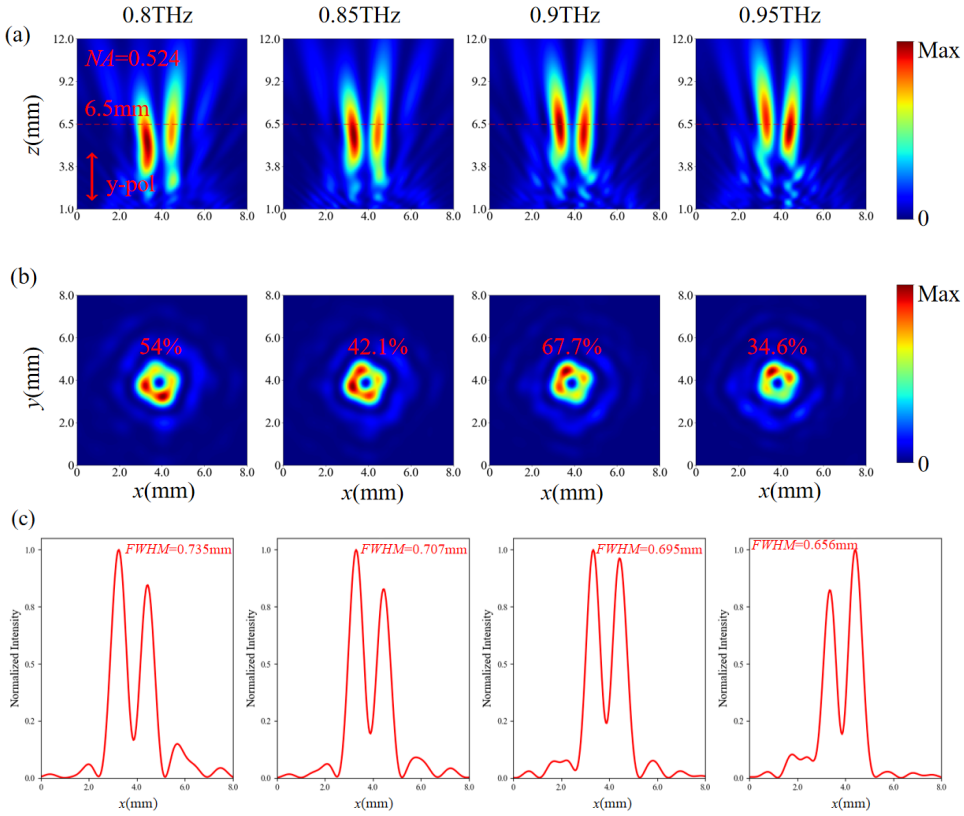


Figure 5. Full-wave simulation results of the designed metasurface under *y*-polarized incidence at different frequencies. (**a**) Energy field distributions in the x–z plane at *y* = 0 mm for different frequencies, showing the focal line (red). (**b**) Energy field distributions in the x–y plane at z = 6.5 mm for different frequencies, with the corresponding focusing efficiencies annotated in red. (**c**) *FWHM* and intensity distributions of the Bessel beam at different frequencies.

Focused vortex beams are also an important component of structured light. We further design metasurfaces generating focused vortex beams with different topological charges under different polarization states using the PSO method. The near-field phase distributions are shown in Figure 6. It can be clearly observed that the phase profiles exhibit distinct topological charge characteristics under different polarization states. Under *x*-polarized incidence, the phase varies by 2π over one full azimuthal cycle, corresponding to a topological charge of $l = 1$. In contrast, under y-polarized incidence, the phase accumulates a total variation of 4π over one full cycle, corresponding to a topological charge of $l = 2$. These

results demonstrate that the proposed metasurface can independently encode different OAM modes into orthogonal linear polarization channels.

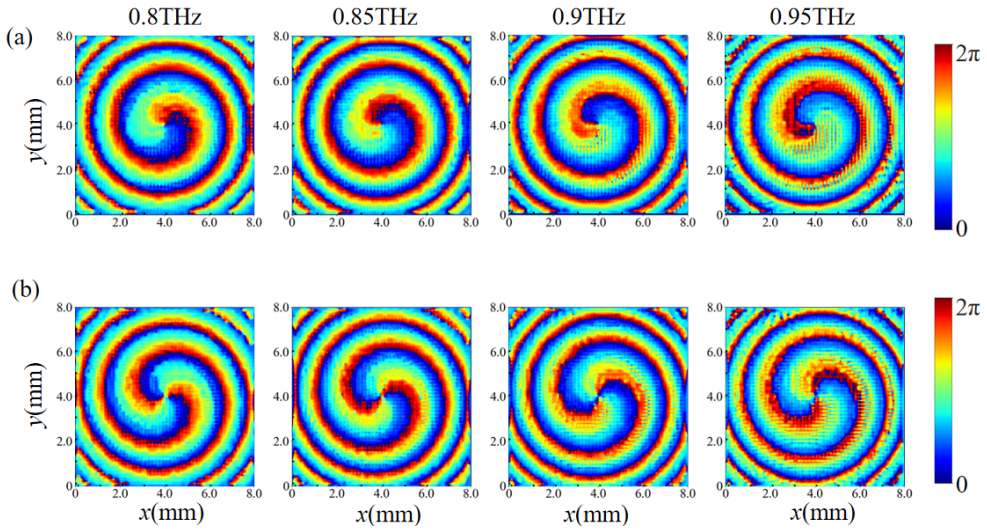


Figure 6. Near-field phase distributions of the metasurface under different polarization states from 0.8 to 0.95 THz obtained by full-wave simulations: (**a**) first-order achromatic focused vortex phase distribution under *x*-polarized incidence; (**b**) second-order achromatic focused vortex phase distribution under *y*-polarized incidence.

Through full-wave simulations, the intensity distribution of the first-order focused vortex beam is obtained, as shown in Figure 7. Within the designed operating bandwidth, the focal peak position of the first-order vortex beam remains stably located at 9 mm, with a *NA* of 0.406. In terms of focusing efficiency, the performance increases from 77.0% at 0.8 THz to a maximum of 82.9% around 0.9 THz, and then decreases to 58.7% at 0.95 THz. The increasing trend in the 0.8–0.9 THz range indicates that the resonance response of the meta-atoms gradually becomes better matched with the target phase profile, leading to improved energy utilization within this frequency band. In contrast, the efficiency drop at 0.95 THz is attributed to the enhanced dielectric dispersion of silicon in the higher THz regime, which results in reduced transmission efficiency and increased phase distortion. The *FWHM* decreases monotonically from 0.416 mm at 0.8 THz to 0.376 mm at 0.95 THz, exhibiting a reduction with decreasing wavelength, which is consistent with diffraction theory predictions.

To further evaluate the focusing quality, we calculate the ratio between the *FWHM* and the corresponding diffraction limit at each frequency point. At 0.8, 0.85, 0.9, and 0.95 THz, the diffraction-limited spot sizes σ are 0.462 mm, 0.435 mm, 0.411 mm, and 0.390 mm, respectively. The actual *FWHM* values are approximately 0.90, 0.89, 0.92, and 0.96 times σ, respectively. It can be seen that all these ratios are smaller than 1, indicating that the transverse resolution of the first-order focused vortex beam approaches the diffraction-limited resolution, demonstrating near-diffraction-limited focusing characteristics.

Under *y*-polarized incidence, the intensity distribution of the second-order focused vortex beam is obtained, as shown in Figure 8. Compared with the first-order vortex, the second-order vortex beam exhibits a weaker phase singularity intensity, i.e., a larger central dark core. This is because, for a topological charge of $l = 2$, the phase accumulates a total variation of 4π around the singularity, leading to an enlarged zero-intensity region at the beam center. The focal peak position of the metasurface under y-polarized incidence remains stably located at 9 mm, with a *NA* of 0.406, consistent with the *x*-polarization channel, which is beneficial for the integrated design of dual-polarization multiplexing systems.

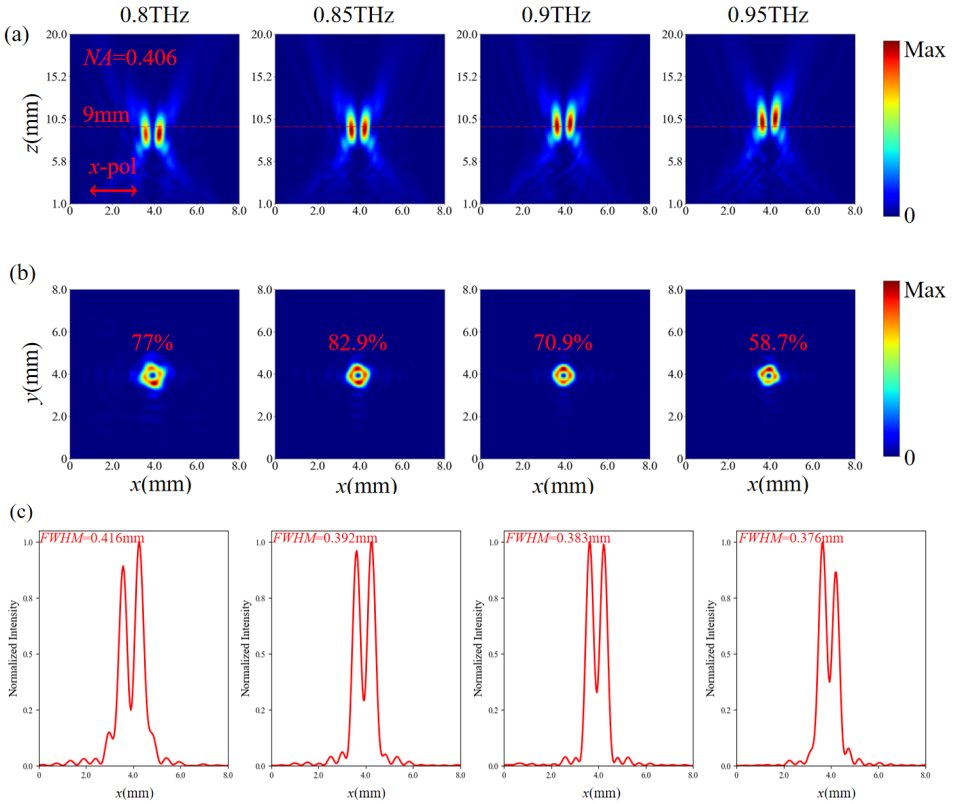


Figure 7. Full-wave simulation results of the designed metasurface under x-polarized incidence at different frequencies. (**a**) Energy field distributions in the x–z plane at y = 0 mm for different frequencies, showing the focal line (red). (**b**) Energy field distributions in the x–y plane at z = 9 mm for different frequencies, with the corresponding focusing efficiencies annotated in red. (**c**) *FWHM* and intensity distributions at different frequencies.

In terms of focusing efficiency, the values at 0.8, 0.85, 0.9, and 0.95 THz are 81.1%, 73.0%, 79.2%, and 64.9%, respectively. The relatively lower efficiency at 0.85 THz (73.0%) and the recovery at 0.9 THz (79.2%) may be attributed to variations in the resonant response of the meta-atoms at different frequencies. Overall, except for 0.95 THz, the efficiency remains above 73% across most of the operating band, indicating high energy utilization. The efficiency drop at 0.95 THz is also attributed to the enhanced dielectric dispersion of silicon in the higher THz regime, consistent with the behavior observed in the first-order vortex case. The *FWHM* at 0.8, 0.85, 0.9, and 0.95 THz is 0.446 mm, 0.435 mm, 0.430 mm, and 0.398 mm, respectively, showing a monotonic decrease with increasing frequency, consistent with diffraction theory predictions. Compared with the diffraction limit $\sigma = \lambda/(2NA)$ (NA = 0.406, with λ = 0.375, 0.3529, 0.3333, and 0.3158 mm, corresponding to the four frequencies, yielding σ = 0.462, 0.435, 0.411, and 0.390 mm), the ratios $FWHM/\sigma$ are 0.97, 1.00, 1.05, and 1.02, respectively. It can be seen that all values are close to 1, indicating that the transverse resolution of the second-order vortex beam approaches the diffraction limit. This is slightly weaker than the first-order vortex (where $FWHM/\sigma < 1$), which is consistent with the physical characteristics of higher-order vortex beams, where an enlarged central dark core leads to a more dispersed energy distribution.

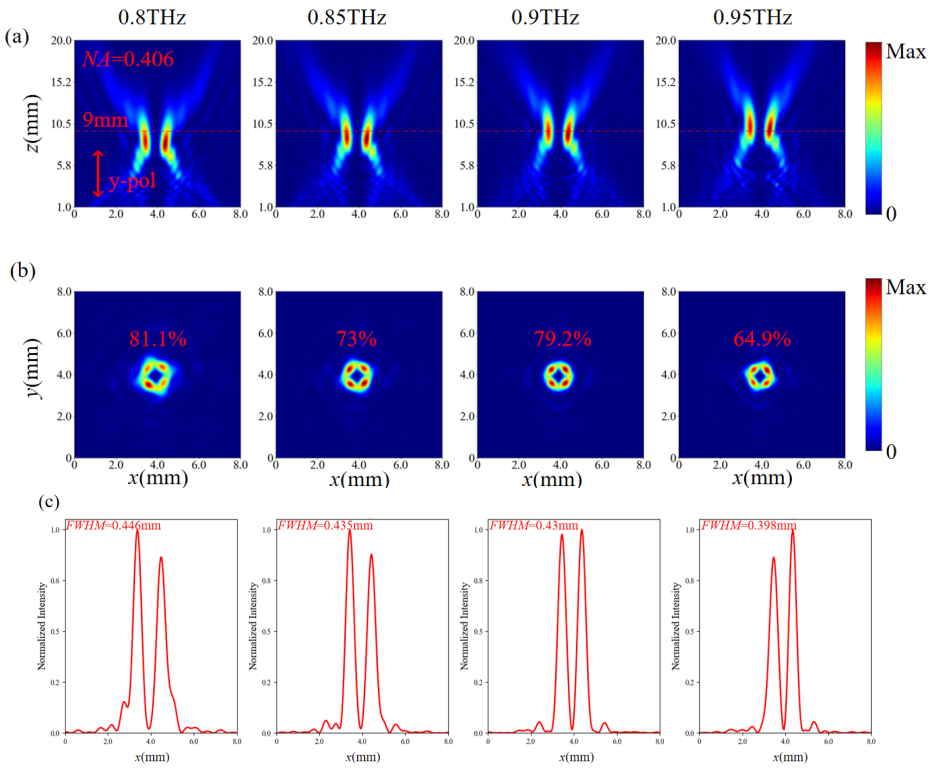


Figure 8. Full-wave simulation results of the designed metasurface under y-polarized incidence at different frequencies. (**a**) Energy field distributions in the x–z plane at y = 0 mm for different frequencies, showing the focal line (red). (**b**) Energy field distributions in the x–y plane at z = 9 mm for different frequencies, with the corresponding focusing efficiencies annotated in red. (**c**) *FWHM* and intensity distributions at different frequencies.

4. Conclusions

We proposes and designs a terahertz achromatic polarization-multiplexed structured light metasurface based on the PSO algorithm, operating over a broadband range from 0.8 THz to 0.95 THz. Using all-dielectric silicon materials and a transmission-phase modulation mechanism, the PSO algorithm is employed to globally optimize the phase compensation coefficients of the metasurface unit cells. This enables the simultaneous satisfaction of distinct phase profiles under orthogonal linear polarization channels while maintaining achromatic performance over a wide frequency band. Based on this design strategy, two types of achromatic polarization-multiplexed structured light metasurfaces are realized. The first type generates a conventional focused spot under x-polarized incidence, with a stable focal position at 8.5 mm and a *NA* of 0.426. The focusing efficiency exceeds 70% within the 0.8–0.9 THz range (except 61.9% at 0.95 THz), and the *FWHM* ranges from 1.00 mm to 0.85 mm. Under y-polarized incidence, a first-order Bessel beam is generated with a focal position at 6.5 mm and a larger *NA* of 0.524. The efficiency varies from 67.7% at 0.8 THz to 34.6% at 0.95 THz, while the central spot *FWHM* ranges from 0.656 mm to 0.735 mm, preserving a nondiffracting core. Both channels exhibit excellent achromatic behavior across all operating frequencies.

The second type generates vortex beams with topological charges of l = 1 under x-polarized incidence and l = 2 under y-polarized incidence. Full-wave simulation results show that the focal peak positions for both channels remain stably located at 9 mm, with a numerical aperture of 0.406. For the x-polarized l = 1 channel, the focusing efficiency increases from 77.0% at 0.8 THz to 82.9% at 0.9 THz, decreasing to 58.7% at 0.95 THz. The *FWHM* decreases from 0.416 mm to 0.376 mm, remaining below the diffraction limit and demonstrating near-diffraction-limited focusing characteristics. For the y-polarized l = 2

channel, the efficiencies are 81.1%, 73.0%, 79.2%, and 64.9%, with *FWHM* ranging from 0.446 mm to 0.398 mm, closely approaching the diffraction limit. In both cases, the phase singularities of the vortex beams remain well preserved.

Although a reduction in efficiency is observed at 0.95 THz due to the enhanced dielectric dispersion of silicon at higher terahertz frequencies, the proposed scheme successfully achieves broadband achromatic manipulation of polarization-multiplexed structured light in the terahertz regime. This work provides a compact, stable, and integrable metasurface platform for terahertz orbital angular momentum multiplexing, diffraction-free imaging, and multidimensional information processing. Future improvements may include the use of low-dispersion dielectric materials (e.g., sapphire) or the integration of deep learning-based inverse design methods to further enhance high-frequency efficiency and overall device performance.

Author Contributions: Conceptualization, S.C. and G.Z.; methodology, S.C.; software, G.Z.; validation, S.C., G.Z. and T.J.; writing—original draft preparation, S.C.; writing—review and editing, G.Z.; supervision, T.J. All authors have read and agreed to the published version of the manuscript.

Funding: This work was funded by grant XT2503980011 from the Guangxi Science and Technology Program, grant XT2503960006 from the Guangxi Regional Innovation Capacity Improvement Program, grant 2024YCXS227 from the Innovation Project of Guilin University of Electronic Technology (GUET) Graduate Education, and grant 62265004 from the National Natural Science Foundation of China.

Institutional Review Board Statement: Not applicable.

Informed Consent Statement: Not applicable.

Data Availability Statement: The data presented in this study are available on request from the corresponding author.

Conflicts of Interest: The authors declare no conflicts of interest.

References

1. Al-Naib, I.; Withayachumnankul, W. Recent progress in terahertz metasurfaces. *J. Infrared Millim. Terahertz Waves* **2017**, *38*, 1067–1084. [CrossRef]
2. Zhang, Z.; Zhao, R.; Cong, M.; Qiu, J. Developments of terahertz metasurface biosensors: A literature review. *Nanotechnol. Rev.* **2024**, *13*, 20230182. [CrossRef]
3. Zang, X.; Yao, B.; Chen, L.; Xie, J.; Guo, X.; Balakin, A.V.; Shkurinov, A.P.; Zhuang, S. Metasurfaces for manipulating terahertz waves. *Light Adv. Manuf.* **2021**, *2*, 148–172. [CrossRef]
4. Kim, G.; Kim, Y.; Yun, J.; Moon, S.-W.; Kim, S.; Kim, J.; Park, J.; Badloe, T.; Kim, I.; Rho, J. Metasurface-driven full-space structured light for three-dimensional imaging. *Nat. Commun.* **2022**, *13*, 5920. [CrossRef]
5. Bao, Y.; Ni, J.; Qiu, C. A minimalist single-layer metasurface for arbitrary and full control of vector vortex beams. *Adv. Mater.* **2020**, *32*, 1905659. [CrossRef]
6. Yue, F.; Wen, D.; Xin, J.; Gerardot, B.D.; Li, J.; Chen, X. Vector vortex beam generation with a single plasmonic metasurface. *ACS Photonics* **2016**, *3*, 1558–1563. [CrossRef]
7. Mei, F.; Qu, G.; Sha, X.; Han, J.; Yu, M.; Li, H.; Chen, Q.; Ji, Z.; Ni, J.; Qiu, C.-W.; et al. Cascaded metasurfaces for high-purity vortex generation. *Nat. Commun.* **2023**, *14*, 6410. [CrossRef]
8. Pfeiffer, C.; Grbic, A. Controlling vector Bessel beams with metasurfaces. *Phys. Rev. Appl.* **2014**, *2*, 044012. [CrossRef]
9. Feng, R.; Ratni, B.; Yi, J.; Jiang, Z.; Zhang, H.; de Lustrac, A.; Burokur, S.N. Flexible manipulation of bessel-like beams with a reconfigurable metasurface. *Adv. Opt. Mater.* **2020**, *8*, 2001084. [CrossRef]
10. Cai, B.G.; Li, Y.B.; Jiang, W.X.; Cheng, Q.; Cui, T.J. Generation of spatial Bessel beams using holographic metasurface. *Opt. Express* **2015**, *23*, 7593–7601. [CrossRef]
11. Li, N.; Zheng, S.; He, T.; Zhang, H.; Lyu, Z.; Yang, H.; Yang, Z.; Zhang, L.; Yu, X. A broadband transmissive metasurface for non-diffractive THz OAM multiplexing and communication. *IEEE Trans. Antennas Propag.* **2024**, *72*, 2161–2170. [CrossRef]
12. Li, Z.; Liu, W.; Geng, G.; Li, Z.; Li, J.; Cheng, H.; Chen, S.; Tian, J. Multiplexed nondiffracting nonlinear metasurfaces. *Adv. Funct. Mater.* **2020**, *30*, 1910744. [CrossRef]

13. Zou, X.; Zhou, P.; Chen, L.; Xing, R.; Chen, J. Tunable Trajectory Direction of Longitudinally Polarization-Varying Vector Bessel Beams Using Spin-Multiplexing Metasurfaces. *Phys. Lett. A* **2026**, *583*, 131706. [CrossRef]
14. Bo, H.; Wang, Z.; Zhifang, Q.; Xinning, Y.; Wang, X.; Kaikai, H.; Mingli, S.; Xu, B. Bessel beams generation with biphase transition of vanadium dioxide metasurface. *Phys. Scr.* **2024**, *99*, 095505. [CrossRef]
15. Kuznetsov, A.I.; Brongersma, M.L.; Yao, J.; Chen, M.K.; Levy, U.; Tsai, D.P.; Zheludev, N.I.; Faraon, A.; Arbabi, A.; Yu, N.; et al. Roadmap for optical metasurfaces. *ACS Photonics* **2024**, *11*, 816–865. [CrossRef] [PubMed]
16. Chang, S.; Guo, X.; Ni, X. Optical metasurfaces: Progress and applications. *Annu. Rev. Mater. Res.* **2018**, *48*, 279–302. [CrossRef]
17. Wang, S.; Wu, P.C.; Su, V.-C.; Lai, Y.-C.; Chu, C.H.; Chen, J.-W.; Lu, S.-H.; Chen, J.; Xu, B.; Kuan, C.-H.; et al. Broadband achromatic optical metasurface devices. *Nat. Commun.* **2017**, *8*, 187. [CrossRef]
18. Cheng, S.; Xu, H.; Ye, S.; Xiao, S.; Zhang, W.; Qu, X.; Chen, M.; Huang, W. Physics-embedded autoencoder for solving broadband light field modulation with metasurfaces. *Results Phys.* **2025**, *77*, 108434. [CrossRef]
19. Cheng, S.; Cao, Y.; Yuan, L.; Chen, M.; Huang, W. Physics-inspired autoencoder for inverse design of achromatic polarization-multiplexed varifocal metalenses. *Phys. Scr.* **2025**, *100*, 105951. [CrossRef]
20. Cheng, S.; Chen, M.; Zhang, Y.; Wang, Y. Deep learning-driven multidistance imaging metasurface. In *Proceedings of SPIE, Vol. 13962, AOPC 2025: Micro-Nano Optics*; SPIE: Washington, DC, USA, 2025; pp. 8–12. [CrossRef]
21. Fu, P.; Chen, Z.; Yi, Z.; Cheng, S.; Ahmad, S.; Li, B. Graphene-based terahertz perfect absorber with broadband, wide-angle, and dynamically tunable performance. *Phys. Status Solidi RRL* **2026**, *20*, e70163. [CrossRef]
22. Zeng, N.; Chen, Z.; Yi, Z.; Cheng, S.; Ahmad, S.; Tang, C.; Gao, F.; Li, B. Terahertz multi-band tunable refractive index sensing graphene absorber based on surface plasmon resonance. *Phys. B Condens. Matter* **2026**, *734*, 418608. [CrossRef]
23. Zhang, H.; Chen, Z.; Yi, Z.; Cheng, S.; Ahmad, S.; Tang, C.; Deng, J. Three band THz perfect absorption device based on graphene metasurface structure. *Phys. E* **2026**, *181*, 116542. [CrossRef]
24. Liu, X.; Fan, K.; Shadrivov, I.V.; Padilla, W.J. Experimental realization of a terahertz all-dielectric metasurface absorber. *Opt. Express* **2017**, *25*, 191–201. [CrossRef]
25. Ma, Z.; Hanham, S.M.; Albella, P.; Ng, B.; Lu, H.T.; Gong, Y.; Maier, S.A.; Hong, M. Terahertz all-dielectric magnetic mirror metasurfaces. *ACS Photonics* **2016**, *3*, 1010–1018. [CrossRef]
26. Liu, W.; Yang, Q.; Xu, Q.; Jiang, X.; Wu, T.; Wang, K.; Gu, J.; Han, J.; Zhang, W. Multifunctional all-dielectric metasurfaces for terahertz multiplexing. *Adv. Opt. Mater.* **2021**, *9*, 2100506. [CrossRef]
27. Kowerdziej, R.; Olifierczuk, M.; Salski, B. Tunable negative index metamaterial employing in-plane switching mode at terahertz frequencies. *Liq. Cryst.* **2012**, *39*, 827–831. [CrossRef]
28. Almpanis, E.; Zouros, G.P.; Tsakmakidis, K.L. Active THz metasurfaces for compact isolation. *J. Opt. Soc. Am. B* **2021**, *38*, C191–C197. [CrossRef]
29. Chen, Y.; Ding, Z.; Zhang, M.; Zhou, J.; Li, M.; Zhao, M.; Wang, J. Metasurface parameter optimization of Fano resonance based on a BP-PSO algorithm. *Appl. Opt.* **2021**, *60*, 9200–9204. [CrossRef] [PubMed]
30. Chen, N.; Yang, S.; An, S. A new hybrid algorithm based on PSO and fireworks algorithm for optimal design of metasurface absorber in RF energy harvesting. *IEEE Trans. Magn.* **2024**, *61*, 7200204. [CrossRef]
31. Jiang, S.; Deng, W.; Wang, Z.; Cheng, X.; Tsai, D.P.; Shi, Y.; Zhu, W. Ka-Band metalens antenna empowered by physics-assisted particle swarm optimization (PA-PSO) algorithm. *Opto-Electron. Sci.* **2024**, *3*, 240014. [CrossRef]
32. Coleman, C.J. On the generalization of Snell's law. *Radio Sci.* **2004**, *39*, RS2005. [CrossRef]
33. Su, G.; Du, Z.; Jiang, P.; Liu, Y. High-efficiency wavefront manipulation in thin plates using elastic metasurfaces beyond the generalized Snell's law. *Mech. Syst. Signal Process.* **2022**, *179*, 109391. [CrossRef]
34. Zhang, J.; Zhao, X.; Zheng, Y.; Chen, X. Generalized nonlinear Snell's law at $\chi^{(2)}$ modulated nonlinear metasurfaces: Anomalous nonlinear refraction and reflection. *Opt. Lett.* **2019**, *44*, 431–434. [CrossRef]
35. Yang, H.; Zhang, M.; Chen, W.; Li, Q.; Zhi, W.; Yu, F.; Xiao, G.; Li, J. Particle swarm optimization-driven tomographic metalens for controllable super-resolution focusing. *Appl. Opt.* **2026**, *65*, 1994–2000. [CrossRef]
36. Xu, J.; Yuan, H.; Zhong, Z.; Zhang, B. All-dielectric metasurface based on particle swarm optimization algorithm for generating high-purity vortex pulses. *Opt. Commun.* **2025**, *584*, 131812. [CrossRef]
37. Ding, F.; Chen, Y.; Bozhevolnyi, S.I. Focused vortex-beam generation using gap-surface plasmon metasurfaces. *Nanophotonics* **2020**, *9*, 371–378. [CrossRef]
38. Khonina, S.N.; Kazanskiy, N.L.; Karpeev, S.V.; Butt, M.A. Bessel beam: Significance and applications—A progressive review. *Micromachines* **2020**, *11*, 997. [CrossRef]
39. Cui, C.; Gao, X.; Chen, Z.; Yi, Z.; Cheng, S.; Ahmad, S.; Tang, C.; Deng, J. Transient simulation and optimization of planar heat source system based on finite element method. *Mod. Phys. Lett. B* **2026**, *40*, 2650081. [CrossRef]

40. Wu, K.; Coquet, P.; Wang, Q.J.; Genevet, P. Modelling of free-form conformal metasurfaces. *Nat. Commun.* **2018**, *9*, 3494. [CrossRef] [PubMed]
41. Palik, E.D. (Ed.) *Handbook of Optical Constants of Solids*; Academic Press: Cambridge, MA, USA, 1985. [CrossRef]

Disclaimer/Publisher's Note: The statements, opinions and data contained in all publications are solely those of the individual author(s) and contributor(s) and not of MDPI and/or the editor(s). MDPI and/or the editor(s) disclaim responsibility for any injury to people or property resulting from any ideas, methods, instructions or products referred to in the content.